Chemical Science

ROYAL SOCIETY OF CHEMISTRY

EDGE ARTICLE

View Article Online
View Journal | View Issue

Cite this: *Chem. Sci.*, 2025, **16**, 20865

All publication charges for this article have been paid for by the Royal Society of Chemistry

Cooperative Fe–Ti dual-metal sites for highly efficient photocatalytic non-oxidative methane conversion

Qingyun Zhan,[a] Xiaowei Mu,*[b] Yuxiang Kong,[a] Zhenlu Li,[a] Le Liu,[a] Yumeng Qian,[a] Shuyan Song *[b] and Lu Li *[a]

Received 29th July 2025
Accepted 6th October 2025

DOI: 10.1039/d5sc05677b

rsc.li/chemical-science

Selective methane conversion is a promising low-carbon technology, yet developing catalysts capable of effectively activating inert C–H bonds under mild conditions remains challenging. Here, we designed Fe^{2+}–□–Ti^{4+} dual-metal-sites on the high-activity {012} facets of defective ilmenite ($Fe_{1-x}TiO_{3-x}$-NS). Mechanistic studies revealed that Fe^{2+}–□–Ti^{4+} can be excited to form a long-lived Fe^{3+}–□–Ti^{3+} active state, while surface lattice oxygen stabilizes the reaction intermediates during multistep elementary reactions. This bimetal–oxygen synergistic strategy significantly reduces the activation barrier for C–H bond cleavage to just 0.15 eV, fully blocks the over-dehydrogenation of methyl intermediates, and facilitates C–C bond formation, thereby achieving a favorable non-oxidative methane conversion rate that even surpasses noble metal-supported photocatalysts, with nearly 100% C_{2+} selectivity. This bimetallic-center construction strategy not only provides an efficient and economical pathway for methane conversion but also expands the boundaries of traditional photocatalysts, exhibiting high catalytic activity and product selectivity.

Introduction

Methane (CH_4), the primary constituent of natural gas, shale gas, and combustible ice, serves not only as a widely used fuel but also as a crucial feedstock for energy production and chemical synthesis.[1,2] However, methane's inert nature—characterized by high symmetry, low polarizability, and high ionization potential—necessitates a substantial energy input for activation. Traditional CH_4 conversion methods demand harsh conditions, such as elevated temperatures, strong oxidizers, or highly acidic environments.[3–5] For instance, methane steam reforming is typically conducted at 700–1100 °C, leading to high energy consumption, catalyst degradation, and significant carbon emissions.[6–8] Therefore, there is an urgent need to develop more economical and sustainable methods for methane conversion under mild conditions.

Photocatalytic non-oxidative coupling of methane (NOCM) is an emerging green technology that utilizes only solar energy and methane as inputs. By harnessing photon-induced high-energy charge carriers to pre-activate the C–H bonds in CH_4, this approach reduces the reaction barrier and enables thermodynamically unfavourable reactions under mild conditions.[6,9–12] Previous studies have demonstrated that quantum dot catalysts (SiO_2,[13–15] Al_2O_3,[13–15] and MgO[16]) and zeolite-based catalysts (H-MOR,[17] MCM-41,[18] Zn^+-ZSM-5,[19] and Nb-TS[20]) can activate methane under light irradiation. However, despite considerable research efforts, the improvement in CH_4 conversion has been limited. Noble metals such as Au,[11,21] Pt,[22,23] Pd,[11,24–26] and Ag[27,28] have been shown to significantly enhance electron transfer, facilitating C–H bond cleavage and accelerating methane conversion, but their high cost remains a significant drawback.[29–31] In recent years, constructing frustrated Lewis pairs (FLPs) on semiconductors has emerged as an effective strategy for C–H activation.[32–34] Nevertheless, this method relies on abundant surface hydroxyl groups, which compromises the long-term stability of the catalysts and requires frequent regeneration treatments.

Ilmenite ($FeTiO_3$) is a titanate mineral with a bandgap of 2.5–2.9 eV and antiferromagnetic semiconducting properties, commonly found in the Earth's crust.[35] Its structure consists of alternating FeO_6 and TiO_6 octahedra sharing faces (Fig. S1), with the metal ion valences represented as $Fe^{2+}Ti^{4+}O_3$.[36] Strong interactions between metals and between metals and ligands facilitate electron transfer,[37–39] and studies suggest that iron-titanium oxides can effectively harness solar energy for photocatalysis.[40] Additionally, calculations by Ribeiro[41] indicate that the Fe valence band maximum (VBM) has more occupied states, while the contribution of oxygen to the valence band near the surface is minimal, reducing excessive oxidation of reactants.[25]

[a]*State Key Laboratory of Inorganic Synthesis and Preparative Chemistry, College of Chemistry, Jilin University, Changchun 130012, People's Republic of China. E-mail: luli@jlu.edu.cn*

[b]*State Key Laboratory of Rare Earth Resource Utilization, Changchun Institute of Applied Chemistry, Chinese Academy of Sciences, Changchun 130022, China. E-mail: muxw@ciac.ac.cn; songsy@ciac.ac.cn*

Thus, $FeTiO_3$ shows significant potential for photocatalytic non-oxidative methane conversion.

Here, we report a defect-state ilmenite catalyst, $Fe_{1-x}TiO_{3-x}$-NS, featuring high-activity {012} facets. Surface oxygen vacancies create Fe^{2+}–□–Ti^{4+} dual-metal sites, which can be excited to form a long-lived Fe^{3+}–□–Ti^{3+}. This structure reduces the activation barrier for C–H cleavage and the surface lattice oxygen can stabilize the reaction intermediates. Under light irradiation, the methane conversion rate reached 5456.2 μmol g^{-1} h^{-1}. This work provides guidance for the rational design and construction of photocatalysts for efficient methane conversion without additional heating.

Results and discussion

Photocatalyst characterization

The $Fe_{1-x}TiO_{3-x}$ nanosheet ($Fe_{1-x}TiO_{3-x}$-NS) catalyst was synthesized *via* a two-step process. Initially, $FeTiO_{3-x}$ nanoparticles ($FeTiO_{3-x}$-NP) were prepared using a sol–gel method, followed by hydrothermal treatment to obtain layered $Fe_{1-x}TiO_{3-x}$-NS (Fig. 1a). The presence of vacancies in both catalysts is indicated by the "*x*" in their notation. Transmission electron microscopy (TEM) images showed that $FeTiO_{3-x}$-NP comprises agglomerated nanoparticles with sizes ranging from 20 to 60 nm. High-resolution transmission electron microscopy (HR-TEM) further revealed lattice fringes of 0.275 nm and 0.374 nm, corresponding to the {104} and {012} planes of $FeTiO_3$, respectively (Fig. 1b). Energy-dispersive X-ray spectroscopy (EDX) mapping confirmed the uniform distribution of Fe, Ti, and O elements (Fig. 1c).

Following hydrothermal treatment, scanning electron microscopy (SEM) demonstrated a morphological transformation from particulate to a layered nanosheet structure ($Fe_{1-x}TiO_{3-x}$-NS) (Fig. 1d), designed to reduce steric hindrance during methane adsorption. HR-TEM images of the layered catalyst showed an interlayer spacing of 7.10–7.13 Å. The TEM image shows that the sample exhibits a nanosheet-like structure. The HRTEM image of the selected area displays clear lattice fringes with an interplanar spacing of 0.374 nm, which matches well with the {012} planes of $FeTiO_3$. The measured lattice angles of approximately 86° and 94° are also consistent with the features of the {012} facet. Fast Fourier Transform (FFT) analysis of the same region clearly identifies diffraction spots corresponding to the (012), (1,0,−2), and (−1,−1,0) planes, with a zone axis of [2,−2,1], indicating that the exposed surface of the nanosheets can be assigned to the {012} facet. EDX mapping confirmed the uniform elemental distribution of Fe, Ti, and O within the samples (Fig. 1e). Inductively coupled plasma (ICP) analysis clearly revealed a reduced Fe/Ti molar ratio in $Fe_{1-x}TiO_{3-x}$-NS compared to $FeTiO_{3-x}$-NP (Fig. S2), which can be ascribed to the partial dissolution of iron species during the hydrothermal treatment. X-ray diffraction (XRD) patterns showed that both materials maintain the pure $FeTiO_3$ phase, although $Fe_{1-x}TiO_{3-x}$-NS exhibited decreased crystallinity and weaker diffraction peaks due to the thin layered structure formed in the hydrothermal step (Fig. 1f).

Theoretical analysis showed that the {012} facet has a lower work function (4.02 eV) compared to the {104} facet (4.89 eV), enabling easier electron transfer and potentially promoting more effective methane activation. (Fig. S3). Ultraviolet photoelectron spectroscopy (UPS) measurements confirmed that the work function of $FeTiO_{3-x}$-NP was 5.56 eV, while that of $Fe_{1-x}TiO_{3-x}$-NS was 4.41 eV (Fig. S4), consistent with theoretical calculations. By combining UPS, X-ray photoelectron spectroscopy (XPS) valence band spectra, and UV-visible spectroscopy, the band structure of $Fe_{1-x}TiO_{3-x}$-NS was determined, showing an excellent match with the redox potential required for methane activation (Fig. S5).

The chemical states of the elements in the catalysts were analysed using XPS. From the Fe 2p and Ti 2p spectra, it was evidenced that Fe exists predominantly as Fe^{2+} with a minor presence of Fe^{3+} in both $FeTiO_{3-x}$-NP and $Fe_{1-x}TiO_{3-x}$-NS, while Ti is entirely present as Ti^{4+} (Fig. S6). In the O 1s spectrum of $FeTiO_{3-x}$-NP (Fig. 1g), peaks at 532.7 eV, 531.1 eV, and 528.9 eV were attributed to surface-adsorbed oxygen (O_C), oxygen vacancies (V_O), and lattice oxygen (O_L),[42] respectively. A marked increase in the oxygen vacancy peak was observed in $Fe_{1-x}TiO_{3-x}$-NS.

Theoretical calculations provided further insight, indicating that the formation energy of oxygen vacancies on the {012} facet is 1.18 eV lower than that on the {104} facet, making oxygen vacancies more likely to form on the {012} facet (Fig. S7). Similar trends were observed for Fe vacancies, which also formed more readily on the {012} facet. Together, these experimental and theoretical findings demonstrate that $FeTiO_{3-x}$-NP contains abundant oxygen vacancies, while $Fe_{1-x}TiO_{3-x}$-NS, with exposed {012} facets after hydrothermal treatment, features a higher concentration of both oxygen and iron vacancies.

Based on the structural characteristics summarized above, we constructed surface models of the {104} and {012} facets using density functional theory (DFT). The models containing oxygen vacancies were denoted as {104}-V_O and {012}-V_O, while the {012} facet containing both oxygen and Fe vacancies was denoted as {012}-V_O–V_{Fe}. In the optimized models, we measured the distances between Fe and Ti atoms across the bridging oxygen vacancy. This bridging oxygen vacancy between Fe and Ti atoms defined the Fe–Ti dual-metal sites (designated as Fe^{2+}–□–Ti^{4+}). On the {104} facet without oxygen vacancies, the Fe–Ti distance was 3.89 Å (Fig. S8a); introducing oxygen vacancies ({104}-V_O) slightly increased this distance to 3.96 Å (Fig. 1h). On the {012} facet without oxygen vacancies, the Fe–Ti distance was 3.46 Å (Fig. S8b); after introducing oxygen vacancies ({012}-V_O), the distance decreased to 2.97 Å (Fig. S8c); further introducing Fe vacancies on this facet ({012}-V_O–V_{Fe}) reduced the distance to 2.89 Å (Fig. 1i). The distance between active sites often correlates directly with catalytic activity, as optimal spacing can accelerate reaction rates. These results reveal substantial structural differences in Fe–Ti configurations across the two facets, which may lead to significant variations in methane adsorption and activation.

We investigated the interaction between the catalyst and CH_4 using temperature-programmed desorption of methane (CH_4-TPD). The desorption peaks around 375 K and 550 K

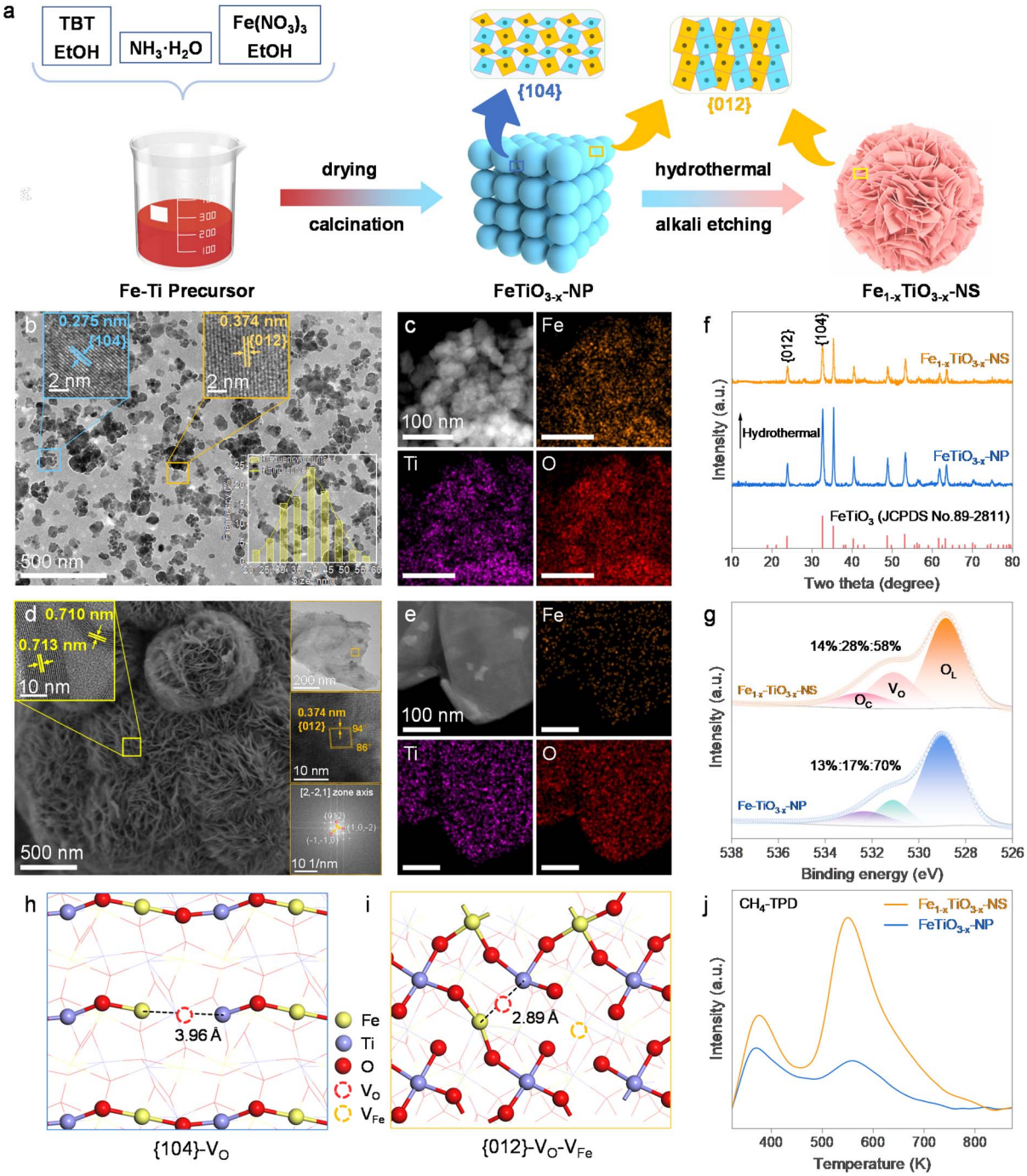

Fig. 1 Structural characterization of the catalyst. (a) Schematic illustration of the synthesis process for $FeTiO_{3-x}$-NP and $Fe_{1-x}TiO_{3-x}$-NS. (b) TEM and HRTEM images of $FeTiO_{3-x}$-NP. (c) EDX elemental mapping of $FeTiO_{3-x}$-NP. (d) SEM, TEM, HRTEM and FFT images of $Fe_{1-x}TiO_{3-x}$-NS. (e) EDX elemental mapping of $Fe_{1-x}TiO_{3-x}$-NS. (f) XRD patterns. (g) XPS spectra of O 1s for $FeTiO_{3-x}$-NP and $Fe_{1-x}TiO_{3-x}$-NS. Note: the V_O peaks observed in the O 1s XPS spectra originate from oxygen atoms adjacent to oxygen vacancies. (h and i) Fe–Ti dual-metal-sites on {104}-V_O (h) and {012}-V_O–V_{Fe} (i). (j) CH_4-TPD profiles of different samples.

corresponded to the weak and strong chemical adsorption of CH_4 on the catalyst surface, respectively.[43] Notably, $Fe_{1-x}TiO_{3-x}$-NS exhibited significantly greater strong adsorption of CH_4 than $FeTiO_{3-x}$-NP (Fig. 1j), with complete desorption requiring a temperature of 840 K, suggesting stronger CH_4 binding to the $Fe_{1-x}TiO_{3-x}$-NS surface. This enhanced strong adsorption can be attributed to $Fe_{1-x}TiO_{3-x}$-NS being almost entirely composed of the highly active {012} facet, which has a higher concentration of oxygen and iron vacancies than the {104} facet.

Photocatalytic NOCM test

We evaluated the performance of the catalysts in photocatalytic non-oxidative coupling of methane (PNOCM) irradiated under

irradiation from a 300 W Xe lamp at room temperature. Ethane and hydrogen were detected as the main products, with trace amounts of propane formed from further ethane coupling. Control experiments ruled out the contributions of thermal catalysis or contamination as carbon sources (Fig. S9). Catalytic activity varied across samples, with C_{2+} production rates ranked as follows: $Fe_{1-x}TiO_{3-x}$-NS > $FeTiO_{3-x}$-NP > c-$FeTiO_3$ > Fe_2TiO_5 > TiO_2 > Fe_2O_3 > Fe_3O_4 (Fig. 2a). At room temperature, $Fe_{1-x}TiO_{3-x}$-NS exhibited the highest activity, yielding 22 times more C_{2+} products than pristine TiO_2 and 6 times more than $FeTiO_{3-x}$-NP. This enhancement was attributed to the dominant exposure of the highly active {012} facets. The activity exhibited a volcano-shaped dependence on processing temperature or duration (Fig. S10), peaking in the sample hydrothermally treated at 453 K for 12 hours. Under Xe lamp irradiation at 293 K, the methane conversion rate reached 645 μmol g^{-1} h^{-1}, with a C_{2+} selectivity of 99.3% (95.1% ethane and 4.2% propane). Without a cold water bath (reaction temperature 377 K, Fig. S11), the methane conversion rate soared to an impressive 5456 μmol g^{-1} h^{-1}, with a C_{2+} selectivity of 95.2% (88.0% ethane and 7.2% propane).

The non-oxidative coupling of methane (NOCM) is thermodynamically unfavourable due to its positive Gibbs free energy. Fig. 2b illustrates the temperature dependence of the NOCM reaction, where the dashed line represents the maximum equilibrium conversion achievable by thermocatalysis, setting a limit above which no thermocatalyst can convert methane. Notably, below 600 K, the theoretical conversion of thermocatalytic methane remains negligible. In contrast, $Fe_{1-x}TiO_{3-x}$-NS achieves a CH_4 conversion rate far exceeding this

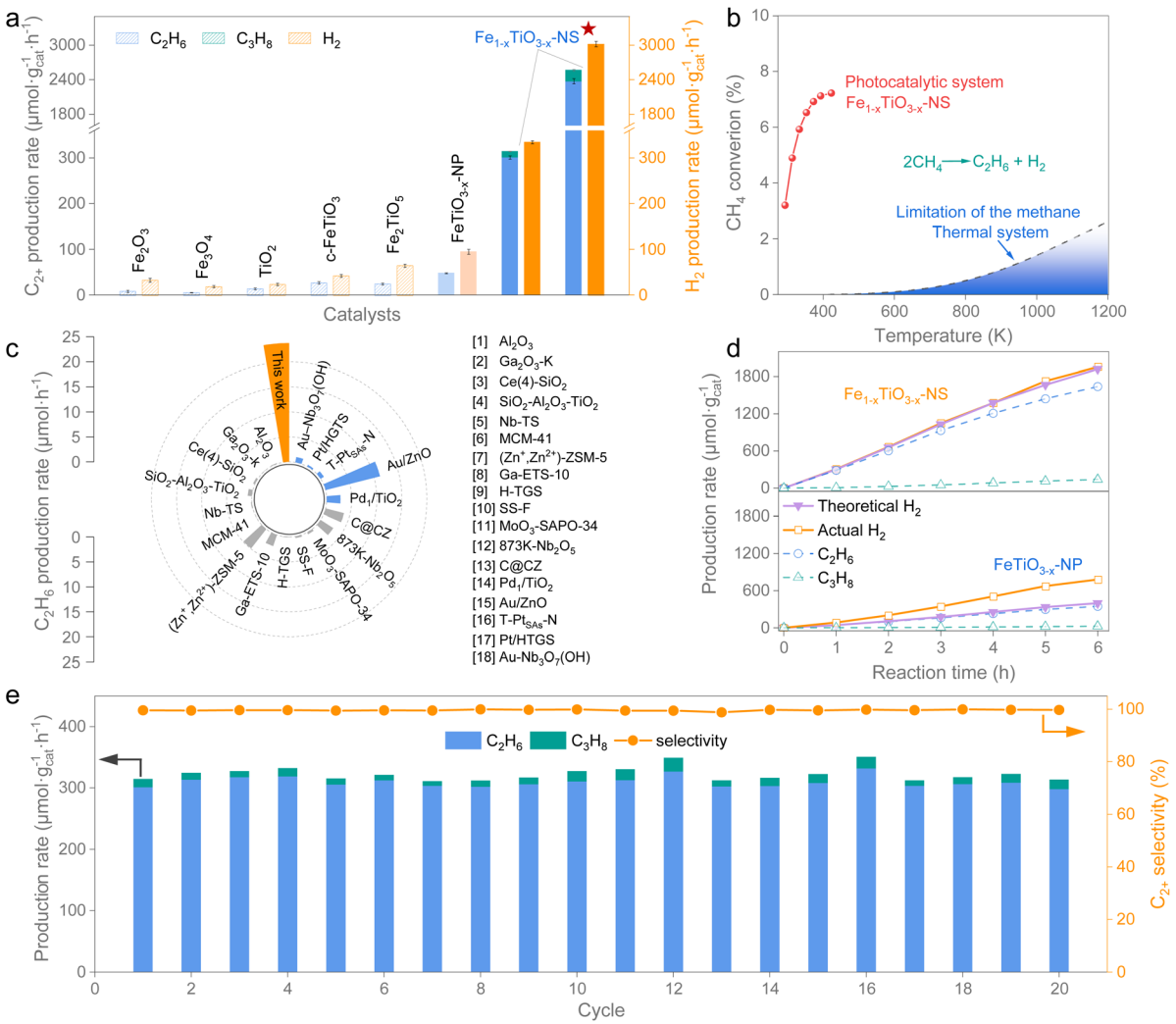

Fig. 2 Photocatalytic NOCM performance. (a) The hydrocarbon products and hydrogen yields over different samples. (b) The limitation of the thermal system for NOCM when using a generic catalyst (dashed line), $Fe_{1-x}TiO_{3-x}$-NS, under light irradiation (yellow dotted line). (c) Summary of C_2H_6 production rates achieved on $Fe_{1-x}TiO_{3-x}$-NS and other reported representative photocatalysts (details in Table S4). (d) Product distribution with reaction time over $Fe_{1-x}TiO_{3-x}$-NS and $FeTiO_{3-x}$-NP samples. (e) The cycling photocatalytic NOCM reactions over $Fe_{1-x}TiO_{3-x}$-NS. Reaction conditions in (a–e): batch quartz reactor; 1.8 mmol CH_4; 10 mg catalyst; irradiated under a 300 W Xe lamp for 2 h. Shown are mean values and error bars are standard deviation. Reaction temperature: (a) 293 K unless specified; [★] 377.4 K without cooling; (b) 293–423 K; (c) 377.4 K; (d and e) 293 K.

thermodynamic limit under illumination at near-room temperature. It is noteworthy that in the lower temperature range (<393 K), the photocatalytic conversion rate significantly increases with rising temperature. However, above 393 K, this temperature effect gradually diminishes, indicating that in a low-temperature gas–solid phase system, heat-limited migration of intermediates and product desorption restrict the turnover frequency of active sites. As the temperature rises, these heat-driven processes accelerate. Once the temperature exceeds 393 K, the rate-determining step shifts to the C–H bond activation process driven by light, rendering further temperature increases ineffective in enhancing the conversion rate.

Fig. 2c compares the performance of $Fe_{1-x}TiO_{3-x}$-NS with a range of reported non-noble metal-based photocatalysts for NOCM. Our catalyst demonstrates a remarkably higher ethane yield, surpassing that of other non-noble metal photocatalysts and even outperforming noble-metal-supported photocatalysts such as Au/ZnO and Pd_1/TiO_2 (Table S4). This exceptional photocatalytic efficiency positions $Fe_{1-x}TiO_{3-x}$-NS as a promising and low-cost candidate for advanced NOCM applications.

We also compared the product distribution over time under light irradiation for both catalysts (Fig. 2d). Apart from C_2H_6, H_2, and C_3H_8, no other products were observed with extended irradiation. The dashed line represents the theoretical hydrogen yield. $Fe_{1-x}TiO_{3-x}$-NS produced hydrogen closely matching the theoretical value, while $FeTiO_{3-x}$-NP produced significantly more hydrogen than expected due to side reactions involving excessive dehydrogenation of CH_4. Raman spectroscopy on the samples after seven reaction cycles (Fig. S12) revealed distinct D and G bands at 1345 cm^{-1} and 1593 cm^{-1} over $FeTiO_{3-x}$-NP, respectively, indicating carbon deposition. In contrast, $Fe_{1-x}TiO_{3-x}$-NS showed no significant D or G bands, suggesting excellent resistance to carbon deposition.

Next, we conducted cyclic testing on both catalysts, with each cycle lasting two hours. Notably, $Fe_{1-x}TiO_{3-x}$-NS maintained consistent activity across 20 cycles, with C_{2+} selectivity remaining above 99% (Fig. 2e), demonstrating not only excellent resistance to sintering but also eliminating the need for regeneration treatments typically required for conventional non-noble metal catalysts. In comparison, the ethane production rate on $FeTiO_{3-x}$-NP dropped to one-fifth of its initial rate after seven cycles, along with a decline in selectivity (Fig. S13). Overall, $Fe_{1-x}TiO_{3-x}$-NS outperforms $FeTiO_{3-x}$-NP in all aspects (Fig. S14). Post-reaction analysis (Fig. S15 and 16) confirmed that both photocatalysts retained their structural integrity, further underscoring their stability.

Photoexcited charge transfer

We employed DFT calculations to simulate the electronic properties of the {012} facet of the catalyst. The projection densities of states (DOSs) for the {012}, {012}-V_O, and {012}-V_O–V_{Fe} facets are shown in Fig. 3a. For the {012} facet, Fe predominantly contributes to the valence band maximum (VBM), suggesting its potential role as an oxidative center

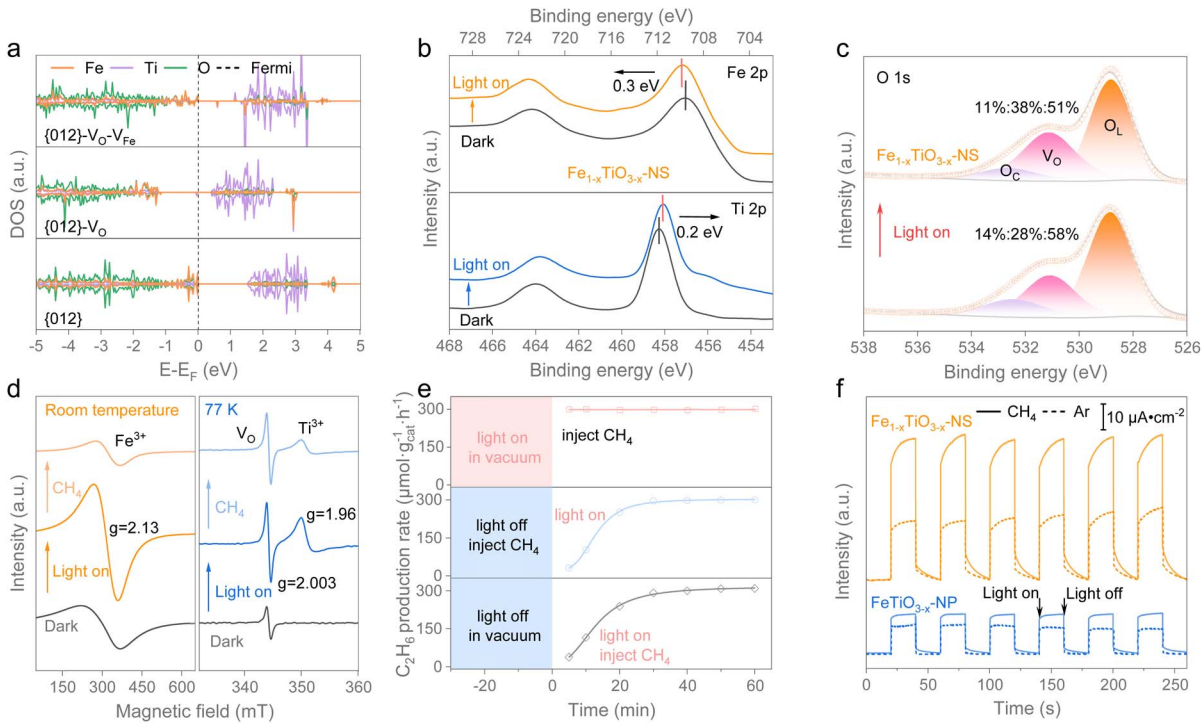

Fig. 3 Investigation of photon-induced charge transfer. (a) The DOS on the {012}, {012}-V_O and {012}-V_O–V_{Fe}. (b) Fe 2p and Ti 2p XPS spectra of $Fe_{1-x}TiO_{3-x}$-NS under light irradiation indicating charge accumulation. (c) *In situ* O 1s XPS spectra for $Fe_{1-x}TiO_{3-x}$-NS catalysts under light illumination. Note: the V_O peaks observed in the O 1s XPS spectra originate from oxygen atoms adjacent to oxygen vacancies. (d) *In situ* EPR signals for the $Fe_{1-x}TiO_{3-x}$-NS catalyst under different conditions. (e) Ethane product rate of $Fe_{1-x}TiO_{3-x}$-NS under different conditions as a function of irradiation time. (f) Photocurrent responses of the as-prepared samples in CH_4 or Ar atmosphere.

through the accumulation of photogenerated holes, while Ti primarily contributes to the conduction band (CB), implying that it may act as a reductive center by accumulating photogenerated electrons during photocatalysis. Introducing oxygen vacancies created new electronic states at the Fermi level, altering the projected DOS and increasing the spin polarization of Ti. When both oxygen and Fe vacancies were introduced, Ti's spin polarization increased further, and Fe also exhibited spin polarization, which helps reduce electron–hole recombination by stabilizing photogenerated charges at active sites. Additionally, these vacancies created new electronic states within the band gap which shortened the electron transition distance and increased carrier concentration, thereby enhancing charge separation efficiency.[44–46] Comparison of the projected DOS of the {104} facet (Fig. S17) revealed a significantly larger band gap than that of the {012} facet, with no defect states introduced by oxygen vacancies. This finding indicates that the charge separation efficiency of the {104}-V_O surface is much lower than that of the {012}-V_O–V_{Fe} facet.

XPS revealed the oxidation state changes of Fe and Ti during photoexcitation. As shown in Fig. 3b and S18, under illumination, the Fe 2p binding energy in $Fe_{1-x}TiO_{3-x}$-NS shifted positively by 0.3 eV, indicating the accumulation of photogenerated holes at Fe sites by the formation of Fe^{3+}. Concurrently, the Ti 2p binding energy shifted negatively by 0.2 eV, suggesting an accumulation of photogenerated electrons at Ti sites, resulting in the formation of Ti^{3+}. These findings align with theoretical predictions. Additionally, the concentration of oxygen vacancies increased under illumination (Fig. 3c), indicating the generation of more Fe–Ti dual-metal sites by photoexcitation. In comparison, $FeTiO_{3-x}$-NP exhibited similar but much smaller changes in Fe, Ti, and oxygen vacancies upon illumination than $Fe_{1-x}TiO_{3-x}$-NS (Fig. S19).

To further analyse electron transfer in $Fe_{1-x}TiO_{3-x}$-NS during the photocatalytic NOCM reaction, we used *in situ* electron paramagnetic resonance (EPR). The EPR signal with $g = 2.13$ measured at room temperature is attributed to Fe^{3+}.[47,48] The signals with $g = 2.003$ and $g = 1.96$, measured at 77 K, are assigned to oxygen vacancies (V_O) and Ti^{3+}, respectively.[23,49,50] As shown in Fig. 3d, after 10 minutes of vacuum illumination, the signals for Fe^{3+} and oxygen vacancies (V_O) increased significantly, and a new signal corresponding to Ti^{3+} emerged, fully consistent with the *in situ* XPS results. When methane was introduced, both the Fe^{3+} and Ti^{3+} signals decreased markedly, suggesting that the photogenerated Fe^{3+} and Ti^{3+} species actively participate in methane activation, facilitating C–H bond cleavage through charge transfer. Notably, after the illumination was removed, the generated Fe^{3+} species remain stable (Fig. S20), indicating that these dual-metal centers effectively inhibit charge transfer from Ti^{3+} to Fe^{3+}. This feature enables the catalyst surface to capture and retain a substantial amount of photogenerated charge, forming a long-lived Fe^{3+}–□–Ti^{3+} active state.

The "Pre-Exposure experiment" further confirmed that $Fe_{1-x}TiO_{3-x}$-NS underwent a photoinduced dynamic transition under illumination from a "resting state" to a long-lived "active state". As shown in Fig. 3e, when the photocatalytic NOCM reaction began immediately after methane introduction, an induction period was observed, during which the catalytic activity of $Fe_{1-x}TiO_{3-x}$-NS increased progressively with extended light exposure, reaching a maximum after approximately 20 minutes before stabilizing (Fig. 3e, bottom). When the catalyst was pre-exposed to methane for 30 minutes before starting the photocatalytic reaction, the induction period persisted (Fig. 3e, middle), indicating that it was not due to CH_4 diffusion or adsorption equilibrium. Conversely, when the catalyst was pre-exposed to light under vacuum for 30 minutes before methane introduction, the NOCM reaction began at the optimal rate without any induction period (Fig. 3e, top). These results collectively underscore that the formation of a long-lived Fe^{3+}–□–Ti^{3+} active state is crucial for methane activation, enabling efficient and sustained photocatalytic performance of $Fe_{1-x}TiO_{3-x}$-NS.

To gain insights into the efficiency of photogenerated charge separation, we conducted photoelectrochemical measurements to investigate interfacial charge dynamics in Ar and CH_4 atmospheres. In the absence of CH_4, $Fe_{1-x}TiO_{3-x}$-NS exhibited a higher photocurrent than $FeTiO_{3-x}$-NP (Fig. 3f), indicating more efficient charge separation and transfer in line with the theoretical calculations and XPS results. When CH_4 was introduced, the photocurrent increased significantly, especially for $Fe_{1-x}TiO_{3-x}$-NS. This surge in photocurrent is attributed to the consumption of photogenerated holes by CH_4, which enhances the transfer of photogenerated electrons to the electrode. These results demonstrate that $Fe_{1-x}TiO_{3-x}$-NS not only facilitates more efficient charge separation but also exhibits a stronger ability to activate methane through enhanced electron transfer dynamics.

Mechanistic investigations

In situ diffuse reflectance infrared Fourier transform spectroscopy (DRIFTS) was employed to investigate the intermediates formed during the PNOCM. Initially, the $Fe_{1-x}TiO_{3-x}$-NS catalyst was exposed to methane in the dark, where a peak at 1302 cm^{-1} was observed, corresponding to the C–H deformation vibration of methane, while the peak at 1541 cm^{-1} was attributed to the symmetric deformation vibration mode of methane on the metal oxide surface.[51,52] Under light irradiation, CH_2/CH_3 deformation vibration modes appeared immediately at 1473 cm^{-1} and 1436 cm^{-1} (Fig. 4a), indicating that CH_4 was rapidly dissociated by photogenerated carriers on $Fe_{1-x}TiO_{3-x}$-NS.[11] Additionally, a C–C stretching peak at 876 cm^{-1} appeared and increased progressively with extended light irradiation, suggesting that C–C coupling occurred on the catalyst surface.[53] Peaks corresponding to C–O (1043 cm^{-1}) and C–O–C (956 cm^{-1}) also emerged under light irradiation, indicating the formation of methoxy species on the catalyst surface, suggesting that they are key intermediates in the PNOCM process on $Fe_{1-x}TiO_{3-x}$-NS.[54,55]

As shown in Fig. 4b, we used DFT to calculate the adsorption energies of CH_4 on the {012}-V_O–V_{Fe}, {104}-V_O, {012}, and {104} facets. The results indicate that on all tested facets, methane preferentially adsorbs at Fe sites. This preference arises from

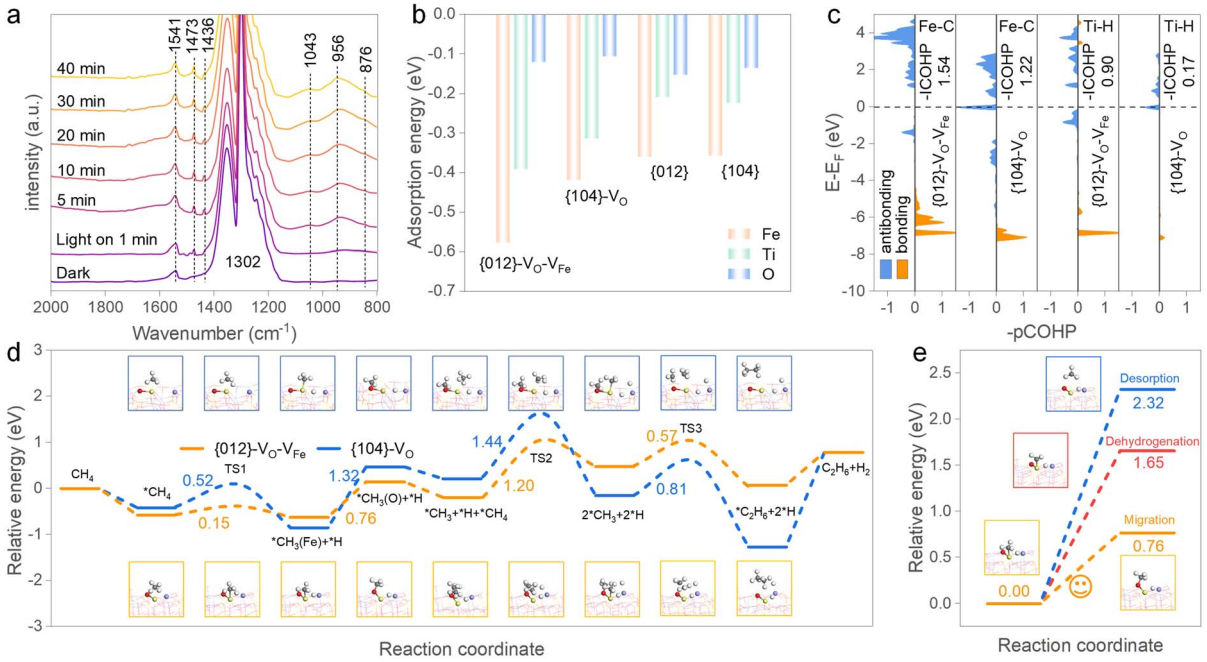

Fig. 4 Investigation of the photocatalytic mechanism. (a) *In situ* DRIFTS spectra for photocatalytic NOCM over $Fe_{1-x}TiO_{3-x}$-NS. (b) The adsorption energy of methane at different sites on different crystal planes. (c) COHPs of CH_4 adsorbed on {012}-V_O–V_{Fe} and {104}-V_O. (d) Free-energy diagrams for C_2H_6 production on {012}-V_O–V_{Fe} and {104}-V_O. (e) Free-energy diagrams for different reaction pathways of methyl on the {012}-V_O–V_{Fe} crystal plane.

the interaction between the d orbitals of Fe and the σ orbitals of CH_4, forming metal–molecule interactions that strengthen CH_4 adsorption on Fe. The optimized adsorption configurations show that the adsorption energy (E_{ads}) of CH_4 on {012}-V_O–V_{Fe} (−0.58 eV) is significantly lower than on {104}-V_O (−0.42 eV), indicating stronger CH_4 adsorption on the {012}-V_O–V_{Fe} facet, consistent with the CH_4-TPD results. Stronger adsorption also led to a lower reaction order for methane on $Fe_{1-x}TiO_{3-x}$-NS (0.44) compared to $FeTiO_{3-x}$-NP (0.51) (Fig. S21).

Analysis of the optimal adsorption configurations indicates that the Fe–□–Ti active sites on the {012}-V_O–V_{Fe} facet exhibit stronger polarization ability for CH_4 adsorption compared to the {104}-V_O facet. As shown in Fig. S22, on the {012}-V_O–V_{Fe} facet, the distance between the Fe site and the carbon atom of methane is 2.29 Å, and the distance between the Ti site and the hydrogen species is 2.91 Å. The C–H bond of CH_4 adsorbed on the catalyst surface is elongated from 1.099 Å in free methane to 1.17 Å. In contrast, on the {104}-V_O facet, the distance between the Fe site and the carbon atom of methane is 2.50 Å, and the distance between the Ti site and the hydrogen species is 3.53 Å, with the C–H bond being elongated to 1.13 Å. We further analysed the projected density of states (PDOS) and projected crystal orbital Hamilton populations (COHP) after CH_4 adsorption (Fig. 4c and S23). The negative integrated COHP (–ICOHP) values for the Fe–C (1.54 eV) and Ti–H (0.90 eV) interactions on the {012}-V_O–V_{Fe} facet are more positive than the Fe–C (1.22 eV) and Ti–H (0.17 eV) interactions on the {104}-V_O facet. All these computational results clearly demonstrate that the Fe–□–Ti active sites on the {012}-V_O–V_{Fe} facet form stronger interactions with methane, which is beneficial for C–H bond cleavage.

To gain a comprehensive understanding of the coupling process in NOCM, we employed DFT to study the reaction pathway of CH_4 on the catalyst surface (Fig. 4d). In the gas phase, C–H bond cleavage requires a large amount of energy (~473 kJ mol^{-1}). However, on the {012}-V_O–V_{Fe} facet, the dissociation of the C–H bond required only 0.15 eV (~14.46 kJ mol^{-1}), significantly lowering the high activation energy barrier typically associated with C–H bond activation. In contrast, on the {104}-V_O facet, the activation energy for the first C–H bond cleavage was much higher, at 0.52 eV, over three times that of the {012}-V_O–V_{Fe} facet. Additionally, the energy required for methyl migration from the Fe site to the adjacent lattice oxygen atom to form the methoxy species intermediate on the {012}-V_O–V_{Fe} surface was 0.76 eV, compared to 1.32 eV on the {104}-V_O surface, indicating that methyl migration proceeds more smoothly on the {012}-V_O–V_{Fe} facet.

Taking spatial effects into account, the activation energy for the second adsorbed CH_4 molecule on the {012}-V_O–V_{Fe} facet was 1.20 eV, higher than that for the first C–H cleavage, but still lower than the 1.44 eV required on the {104}-V_O facet, further demonstrating the superior ability of the {012}-V_O–V_{Fe} facet for C–H bond activation. For ethane formation in the NOCM process, the energy required on the {012}-V_O–V_{Fe} facet was 0.53 eV, compared to 0.81 eV on the {104}-V_O facet, confirming that methane-to-ethane conversion on the {012}-V_O–V_{Fe} facet is more energetically favourable. In terms of hydrogen gas formation, the energy barrier on the {012}-V_O–V_{Fe} facet was only 0.1 eV (Fig. S24), with product desorption requiring 0.33 eV, indicating

that hydrogen can easily desorb from the surface, promoting the overall forward reaction. Moreover, calculations reveal that the cleavage of the C–H of the second adsorbed CH_4 is the rate-determining step in the overall process.

The conversion mechanism of the methyl intermediate is crucial in determining reaction selectivity. We explored the potential reaction pathways of the *in situ* generated methyl intermediate on the catalyst surface. As shown in Fig. 4e, on the {012}-V_O–V_{Fe} facet, the energy required for direct desorption of the methyl intermediates into the gas phase was 2.32 eV, while further dehydrogenation required 1.65 eV. In contrast, the migration of the methyl group from the Fe site to the neighbouring lattice oxygen atom required only 0.76 eV. This energetically favourable migration pathway ensures Fe site regeneration, enabling the adsorption and activation of a second methane molecule, leading to nearly exclusive production of coupling products and complete suppression of carbon deposition. On the {104}-V_O facet, however, as shown in Fig. S25, the more favourable pathway for the methyl intermediate was further dehydrogenation (0.32 eV) rather than migration (1.32 eV), which leads to significant carbon deposition. These theoretical findings align well with the catalytic testing and Raman spectroscopy results. The $FeTiO_{3-x}$-NP sample, composed of a mixture of {012}-V_O–V_{Fe} and {104}-V_O facets, produces excessive hydrogen and large amounts of carbon deposition. In contrast, the $Fe_{1-x}TiO_{3-x}$-NS sample, composed almost entirely of {012}-V_O–V_{Fe} facets, demonstrates nearly 100% C_{2+} product selectivity and stoichiometric hydrogen production, with no significant carbon deposition observed, even after extended cycling.

The photocatalytic NOCM reaction occurring on Fe_{1-x}-TiO_{3-x}-NS is illustrated in Fig. S26. Initially, $Fe_{1-x}TiO_{3-x}$-NS absorbs a photon of light with energy greater than or equal to their bandgap, leading to the generation of photogenerated electron–hole pairs. The photogenerated holes are captured by Fe in the valence band, while the photogenerated electrons are captured by Ti in the conduction band, forming a stable, long-lived activated state. Subsequently, methane molecules are firmly adsorbed onto the catalyst surface, establishing stable molecule–site interactions. This interaction significantly enhances the orbital coupling between methane and the active sites, thereby facilitating the interaction of photogenerated charge carriers with methane and enabling efficient C–H bond cleavage. The generated methyl group preferentially migrates to nearby lattice oxygen, forming a stable methoxy intermediate, which releases the active site and reduces the spatial hindrance for the adsorption of a second methane molecule. Finally, the two methyl groups couple to form ethane, while two hydrogen species couple to form hydrogen gas. The products then desorb from the catalyst surface, completing the catalytic cycle. Throughout the reaction, the bimetallic sites and surface lattice oxygen exhibit a synergistic effect that optimizes the pathways for each elementary step. This includes lowering the activation barriers for both C–H bond cleavages, facilitating methyl migration, reducing the energy barrier for C–C bond formation, and suppressing further dehydrogenation of the methyl group. Compared to conventional active centers, this bimetal–oxygen synergistic strategy significantly enhances both catalytic activity and product selectivity.

Conclusions

In summary, this study demonstrates that the unique bimetal–oxygen active centers on the {012}-V_O–V_{Fe} facet of defective ilmenite nanosheets exhibit a synergistic effect throughout photocatalytic NOCM. By generating long-lived excited states at different stages of methane conversion, these centers achieve remarkable catalytic performance by reducing activation barriers, stabilizing intermediates, and selectively steering reaction pathways, effectively preventing carbon deposition. This bimetal–oxygen synergistic strategy offers a promising pathway for designing high-efficiency, economical catalysts that resolve the traditional trade-off between activity and selectivity. Overall, this work marks an advancement in methane valorization under mild conditions and broadens the scope of heterogeneous catalysis for sustainable fuel and chemical synthesis.

Author contributions

Q. Z., X. M., S. S., and L. L. conceived and designed the project. Q. Z. and X. M. L. L. performed the experiments, analysed the data and wrote the manuscript. Q. Z. and Y. K. co-performed the DFT calculations. Z. L., L. L. and Y. Q. gave suggestions on the research. All authors commented on the manuscript.

Conflicts of interest

There are no conflicts to declare.

Data availability

The data supporting this article have been included as part of the supplementary information (SI). Supplementary information: experimental details, characterizations, supplementary photocatalytic performance tests, and mechanistic studies. See DOI: **https://doi.org/10.1039/d5sc05677b**.

Acknowledgements

This work was financially supported by the National Natural Science Foundation (NSFC) of China (Grant No. 22379050, 22025506), the National Key Research and Development Program of China (2023YFA1506300), the Science and Technology Development Plan Project of Changchun, China (2024GZZ01), the Natural Science Foundation of Jilin Province (20240302098GX), and the Fundamental Research Funds for the Central Universities.

Notes and references

1 D. Saha, H. A. Grappe, A. Chakraborty and G. Orkoulas, *Chem. Rev.*, 2016, **116**, 11436–11499.

2 D. Kiani, S. Sourav, Y. Tang, J. Baltrusaitis and I. E. Wachs, *Chem. Soc. Rev.*, 2021, **50**, 1251–1268.
3 X. Guo, G. Fang, G. Li, H. Ma, H. Fan, L. Yu, C. Ma, X. Wu, D. Deng, M. Wei, D. Tan, R. Si, S. Zhang, J. Li, L. Sun, Z. Tang, X. Pan and X. Bao, *Science*, 2014, **344**, 616–619.
4 P. Schwach, X. Pan and X. Bao, *Chem. Rev.*, 2017, **117**, 8497–8520.
5 C. Díaz-Urrutia and T. Ott, *Science*, 2019, **363**, 1326–1329.
6 X. Meng, X. Cui, N. P. Rajan, L. Yu, D. Deng and X. Bao, *Chem*, 2019, **5**, 2296–2325.
7 H. Song, X. Meng, Z. Wang, H. Liu and J. Ye, *Joule*, 2019, **3**, 1606–1636.
8 Y. Song, E. Ozdemir, S. Ramesh, A. Adishev, S. Subramanian, A. Harale, M. Albuali, B. A. Fadhel, A. Jamal, D. Moon, S. H. Choi and C. T. Yavuz, *Science*, 2020, **367**, 777–781.
9 L. Yuliati and H. Yoshida, *Chem. Soc. Rev.*, 2008, **37**, 1592–1602.
10 L. Li, G.-D. Li, C. Yan, X.-Y. Mu, X.-L. Pan, X.-X. Zou, K.-X. Wang and J.-S. Chen, *Angew. Chem., Int. Ed.*, 2011, **50**, 8299–8303.
11 W. Jiang, J. Low, K. Mao, D. Duan, S. Chen, W. Liu, C.-W. Pao, J. Ma, S. Sang, C. Shu, X. Zhan, Z. Qi, H. Zhang, Z. Liu, X. Wu, R. Long, L. Song and Y. Xiong, *J. Am. Chem. Soc.*, 2021, **143**, 269–278.
12 X. Li, C. Wang and J. Tang, *Nat. Rev. Mater.*, 2022, **7**, 617–632.
13 Y. Kato, H. Yoshida and T. Hattori, *Chem. Commun.*, 1998, **130**, 2389–2390.
14 H. Yoshida, N. Matsushita, Y. Kato and T. Hattori, *Phys. Chem. Chem. Phys.*, 2002, **4**, 2459–2465.
15 H. Yoshida, N. Matsushita, Y. Kato and T. Hattori, *J. Phys. Chem. B*, 2003, **107**, 8355–8362.
16 L. Yuliati, T. Hattori and H. Yoshida, *Phys. Chem. Chem. Phys.*, 2005, **7**, 195–201.
17 Y. Kato, H. Yoshida, A. Satsuma and T. Hattori, *Microporous Mesoporous Mater.*, 2002, **51**, 223–231.
18 L. Yuliati, M. Tsubota, A. Satsuma, H. Itoh and H. Yoshida, *J. Catal.*, 2006, **238**, 214–220.
19 L. Li, Y.-Y. Cai, G.-D. Li, X.-Y. Mu, K.-X. Wang and J.-S. Chen, *Angew. Chem., Int. Ed.*, 2012, **51**, 4702–4706.
20 Z. Chen, S. Wu, J. Ma, S. Mine, T. Toyao, M. Matsuoka, L. Wang and J. Zhang, *Angew. Chem., Int. Ed.*, 2021, **60**, 11901–11909.
21 L. Meng, Z. Chen, Z. Ma, S. He, Y. Hou, H.-H. Li, R. Yuan, X.-H. Huang, X. Wang, X. Wang and J. Long, *Environ. Sci. Technol.*, 2018, **11**, 294–298.
22 S. Q. Wu, X. J. Tan, J. Y. Lei, H. Chen, L. Wang and J. Zhang, *J. Am. Chem. Soc.*, 2019, **141**, 6592–6600.
23 L. Zhang, L. Liu, Z. Pan, R. Zhang, Z. Gao, G. Wang, K. Huang, X. Mu, F. Bai, Y. Wang, W. Zhang, Z. Cui and L. Li, *Nat. Energy*, 2022, **7**, 1042–1051.
24 S. P. Singh, A. Yamamoto, E. Fudo, A. Tanaka, H. Kominami and H. Yoshida, *ACS Catal.*, 2021, **11**, 13768–13781.
25 W. Zhang, C. Fu, J. Low, D. Duan, J. Ma, W. Jiang, Y. Chen, H. Liu, Z. Qi, R. Long, Y. Yao, X. Li, H. Zhang, Z. Liu, J. Yang, Z. Zou and Y. Xiong, *Nat. Commun.*, 2022, **13**, 2806.
26 C. Tang, S. Du, H. Huang, S. Tan, J. Zhao, H. Zhang, W. Ni, X. Yue, Z. Ding, Z. Zhang, R. Yuan, W. Dai, X. Fu, M. B. J. Roeffaers and J. Long, *ACS Catal.*, 2023, **13**, 6683–6689.
27 X. Yu, V. L. Zholobenko, S. Moldovan, D. Hu, D. Wu, V. V. Ordomsky and A. Y. Khodakov, *Nat. Energy*, 2020, **5**, 511–519.
28 J. Zhang, J. Shen, D. Li, J. Long, X. Gao, W. Feng, S. Zhang, Z. Zhang, X. Wang and W. Yang, *ACS Catal.*, 2023, **13**, 2094–2105.
29 Z. Liang, T. Li, M. Kim, A. Asthagiri and J. F. Weaver, *Science*, 2017, **356**, 299–303.
30 D. Li, Y. Zhao, C. Zhou, L.-P. Zhang, J. Tang and T. Zhang, *Fundam. Res.*, 2024, **4**, 934–940.
31 X. Liu, Y. Ling, C. Sun, H. Shi, H. Zheng, C. Song, K. Gao, C. Dang, N. Sun, Y. Xuan and Y. Ding, *Fundam. Res.*, 2024, **4**, 131–139.
32 J. Ma, Q. Zhang, Z. Chen, K. Kang, L. Pan, S. Wu, C. Chen, Z. Wu, J. Zhang and L. Wang, *Chem Catal.*, 2022, **2**, 1775–1792.
33 Z. Chen, Y. Ye, X. Feng, Y. Wang, X. Han, Y. Zhu, S. Wu, S. Wang, W. Yang, L. Wang and J. Zhang, *Nat. Commun.*, 2023, **14**, 2000.
34 R. Song, G. Zhao, J. M. Restrepo-Flórez, C. J. Viasus Pérez, Z. Chen, C. Ai, A. Wang, D. Jing, A. A. Tountas, J. Guo, C. Mao, C. Li, J. Shen, G. Cai, C. Qiu, J. Ye, Y. Fu, C. T. Maravelias, L. Wang, J. Sun, Y.-F. Xu, Z. Li, J. Y. Y. Loh, N. T. Nguyen, L. He, X. Zhang and G. A. Ozin, *Nat. Energy*, 2024, **9**, 750–760.
35 S. E. Haggerty and V. Sautter, *Science*, 1990, **248**, 993–996.
36 X. Tang, K.-a. Hu, X. Tang and K.-a. Hu, *J. Mater. Sci.*, 2006, **41**, 8025–8028.
37 D. M. Sherman and D. M. Sherman, *Phys. Chem. Miner.*, 1987, **14**, 355–363.
38 S. M. Butorin, J.-H. Guo, M. Magnuson and J. Nordgren, *Phys. Rev. B:Condens. Matter Mater. Phys.*, 1997, **55**, 4242–4249.
39 T. Seda, G. R. Hearne, T. Seda and G. R. Hearne, *J. Phys.:Condens. Matter*, 2004, **16**, 2707–2718.
40 M. O. J. Y. Hunault, W. Khan, J. Minár, T. Kroll, D. Sokaras, P. Zimmermann, M. U. Delgado-Jaime and F. M. F. d. Groot, *Inorg. Chem.*, 2017, **56**, 10882–10892.
41 R. A. P. Ribeiro, A. Camilo and S. R. de Lazaro, *J. Magn. Magn. Mater.*, 2015, **394**, 463–469.
42 X. Luo, L. Zhang, X. Gong, Y. Liu and J. Tian, *Chem. Eng. Sci.*, 2023, **280**, 119068.
43 H. Xiong, Y. Dong, C. Hu, Y. Chen, H. Liu, R. Long, T. Kong and Y. Xiong, *J. Am. Chem. Soc.*, 2024, **146**, 9465–9475.
44 V. S. Bystrov, C. Piccirillo, D. M. Tobaldi, P. M. L. Castro, J. Coutinho, S. Kopyl and R. C. Pullar, *Appl. Catal., B*, 2016, **196**, 100–107.
45 T. Ling, D.-Y. Yan, Y. Jiao, H. Wang, Y. Zheng, X. Zheng, J. Mao, X.-W. Du, Z. Hu, M. Jaroniec, S.-Z. Qiao, T. Ling, D.-Y. Yan, Y. Jiao, H. Wang, Y. Zheng, X. Zheng, J. Mao, X.-W. Du, Z. Hu, M. Jaroniec and S.-Z. Qiao, *Nat. Commun.*, 2016, **7**, 12876.
46 X. Lin, S. Xia, L. Zhang, Y. Zhang, S. Sun, Y. Chen, S. Chen, B. Ding, J. Yu and J. Yan, *Adv. Mater.*, 2022, **34**, 2200756.

47 S. P. Balena, I. Messerschmidt, J. C. Tomazoni, E. Guimarães, B. F. Pereira, F. J. Ponzoni, W. E. H. Blum and A. S. Mangrich, *J. Braz. Chem. Soc.*, 2011, **22**, 1788–1794.
48 N. Pathak, S. K. Gupta, K. Sanyal, M. Kumar, R. M. Kadam and V. Natarajan, *Dalton Trans.*, 2014, **43**, 9313–9323.
49 F. Zuo, L. Wang, T. Wu, Z. Zhang, D. Borchardt and P. Feng, *J. Am. Chem. Soc.*, 2010, **132**, 11856–11857.
50 H. Li, J. Chen, Z. Xia and J. Xing, *J. Mater. Chem. A*, 2014, **3**, 699–705.
51 C. Li and Q. Xin, *J. Phys. Chem. C*, 2002, **96**, 7714–7718.
52 X. Yu, V. De Waele, A. Löfberg, V. Ordomsky, A. Y. Khodakov, X. Yu, V. De Waele, A. Löfberg, V. Ordomsky and A. Y. Khodakov, *Nat. Commun.*, 2019, **10**, 700.
53 K. S. Finnie, V. Luca, P. D. Moran, J. R. Bartlett and J. L. Woolfrey, *J. Mater. Chem.*, 2000, **10**, 409–418.
54 A. Yee, S. J. Morrison and H. Idriss, *J. Catal.*, 1999, **186**, 279–295.
55 K. Kähler, M. C. Holz, M. Rohe, J. Strunk and M. Muhler, *ChemPhysChem*, 2010, **11**, 2521–2529.